RESEARCH ARTICLE | FEBRUARY 25 2026

Modulating non-radiative recombination related to shallow traps in halide perovskites

Special Collection: Frontiers in energy materials research: novel measurement, modelling and processing approaches

Dengyang Guo ; Alan R. Bowman ; Sebastian Gorgon ; Changsoon Cho ; Young-Kwang Jung ; Jiashang Zhao ; Linjie Dai ; Jaewang Park ; Kyung Mun Yeom; Satyawan Nagane ; Stuart Macpherson; Weidong Xu ; Jun Hong Noh; Sang Il Seok; Tom Savenije ; Samuel D. Stranks

Appl. Phys. Rev. 13, 011419 (2026)
https://doi.org/10.1063/5.0279622

Applied Physics Reviews ARTICLE pubs.aip.org/aip/are

Modulating non-radiative recombination related to shallow traps in halide perovskites

Cite as: Appl. Phys. Rev. **13**, 011419 (2026); doi: 10.1063/5.0279622
Submitted: 7 May 2025 · Accepted: 16 December 2025 ·
Published Online: 25 February 2026

Dengyang Guo,[1,2] Alan R. Bowman,[1,2,3] Sebastian Gorgon,[1] Changsoon Cho,[1,4,5] Young-Kwang Jung,[2] Jiashang Zhao,[6] Linjie Dai,[1,2] Jaewang Park,[7] Kyung Mun Yeom,[8] Satyawan Nagane,[2] Stuart Macpherson,[1] Weidong Xu,[2] Jun Hong Noh,[8,9] Sang Il Seok,[7] Tom Savenije,[6] and Samuel D. Stranks[1,2,a)]

AFFILIATIONS

[1]Department of Physics, Cavendish Laboratory, University of Cambridge, Cambridge, United Kingdom
[2]Department of Chemical Engineering and Biotechnology, University of Cambridge, Cambridge, United Kingdom
[3]Laboratory of Nanoscience for Energy Technologies, STI, École Polytechnique Fédérale de Lausanne, Lausanne, Switzerland
[4]Department of Material Science and Engineering, Pohang University of Science and Technology (POSTECH), Pohang, Republic of Korea
[5]Institute for Convergence Research and Education in Advanced Technology, Yonsei University, Seoul, Republic of Korea
[6]Department of Chemical Engineering, Delft University of Technology, Delft, the Netherlands
[7]Department of Energy and Chemical Engineering, Ulsan National Institute of Science and Technology (UNIST), Ulsan, Korea
[8]School of Civil, Environmental and Architectural Engineering, Korea University, Seoul, Republic of Korea
[9]Department of Integrative Energy Engineering, Korea University & Graduate School of Energy and Environment (KU-KIST Green School), Korea University, Seoul, Republic of Korea

Note: This paper is part of the APR Special Topic on Frontiers in energy materials research: Novel measurement, modelling and processing approaches.

[a)]**Author to whom correspondence should be addressed:** sds65@cam.ac.uk

ABSTRACT

Halide perovskite solar cells have demonstrated a rapid increase in power conversion efficiencies. Understanding and mitigating remaining carrier losses in halide perovskites is now crucial to enable further increases to approach their practical efficiency limits. Recent observations in halide perovskites have revealed processes such as shallow carrier trapping, which give rise to an apparent non-radiative bimolecular channel that is difficult to distinguish from intrinsic radiative recombination. Here, we quantify this shallow-trap manifestation by jointly analyzing time-resolved photoluminescence and quantum efficiency to separate the total second-order term into radiative ($\eta_{esc}k_{2r}$) and shallow-trap-mediated non-radiative contributions (k_{2non}), and evaluate their device impact. We show that k_{2non} is strongly modulated by temperature and surface chemistry and thus depends on extrinsic factors and its origin is independent from deep traps, whereas the intrinsic radiative coefficient and intrinsic second-order recombination follow detailed-balance expectations and align with theoretical evaluations through van Roosbroeck–Shockley relations. Based on density functional theory simulations and Quasi-Fermi level calculations, we propose that surface states are the primary origin of this shallow-trap-related second-order component, contributing up to ~80 mV of the overall reduction in V_{oc} at room temperature. This work reveals that the origin of carrier losses from two non-radiative recombination types (first and second order) are not linked, emphasizing the need for distinctive mitigation strategies targeting each type to unlock the full efficiency potential of perovskite solar cells.

I. INTRODUCTION

Halide perovskite solar cells have emerged as a promising candidate for next-generation photovoltaics due to their excellent optoelectronic properties and rapid progress in power conversion efficiencies. With reported efficiencies now reaching 27%,[1] perovskite solar cells have already demonstrated their potential to compete with efficiencies of traditional silicon-based technologies. To drive down power conversion losses to their lowest possible values and approach their practical

limits, a complete understanding of charge carrier recombination dynamics for solar cells is crucial, regardless of the choice of absorber materials.

In all solar cells, the theoretical maximum efficiency—governed by the Shockley–Queisser (SQ) limit—assumes idealized conditions, including perfect charge extraction and no non-radiative recombination losses.[2–5] However, in practical devices, material imperfections in the absorber layer (e.g., bulk and surface recombination) impose a lower, practical efficiency limit. This limit reflects the best performance achievable with existing absorber materials under realistic constraints. While optimizing charge transport layers and electrode contacts can reduce resistive losses and improve device performance, such enhancements cannot surpass the practical efficiency limit inherently defined by the absorber's non-ideal properties. Thus, advancing the absorber material itself remains critical for bridging the gap between practical and theoretical efficiencies.[2,6] These losses are attributed to non-radiative carrier recombination, which can typically (for example, in halide perovskites) be categorized as first-order, second-order, or third-order processes, depending on the excitation density. Typically, non-radiative carrier losses in halide perovskites have been linked to first-order trap-assisted recombination, which is dominant at low charge carrier densities and characterized by coefficient k_1, or to third-order Auger recombination, which prevails at high charge carrier densities (typically beyond the operational regimes of solar cells). However, at operating charge carrier densities, second-order processes are frequently dominant (especially once first-order charge trapping has been minimized) and typically considered radiative, represented by coefficient k_{2r}. This process is often referred to as band-to-band or radiative recombination between free electrons and holes, an intrinsic property of semiconductors, while first-order processes depend on extrinsic factors.

A growing body of work reports shallow traps near the band edges in halide perovskites, for example, through long-lived tail components in time-resolved photoluminescence (TRPL) transients at device-relevant excitation densities. These works collectively reveal carrier-loss dynamics that are consistent with an apparent non-radiative contribution to the bimolecular term that is difficult to distinguish from intrinsic radiative recombination.[2–4] Early demonstrations separated the radiative vs non-radiative shares of the measured second-order term using outcoupling/photon-recycling control together with TRPL/transient absorption (TA)/photoluminescence quantum efficiency (PLQE) models,[3,5] and time-resolved microwave photoconductivity (TRMC)/PLQE analyses quantified a non-radiative share.[6] Here, we directly separate the radiative component from a shallow-trap-mediated non-radiative component, demonstrate its temperature- and passivation-dependent modulation, and assess its device-level significance.[7–9]

In this framework, we introduce the notation k_{2non} to denote the non-radiative share of the total second-order coefficient k_2, which we will later relate to a shallow-trap manifestation, distinct from the intrinsic radiative k_{2r} and the first-order SRH term k_1 (see supplementary material note 1). Such a shallow-trap manifestation means the overall second-order recombination with rate k_2 is not equal to the radiative rate k_{2r}, but rather $k_2 = \eta_{esc}k_{2r} + k_{2non}$, accounting for both radiative and non-radiative second-order processes. Here, η_{esc} stands for the escape probability of photons from the film, including the effect of photon recycling. Despite previous studies separating radiative and non-radiative contributions to the experimentally extracted k_2[3,6,7,9] and identifying shallow band edge trap states in halide perovskites,[2,6,10] a direct quantitative link between k_{2non} and specific shallow-trap populations—and how this contribution can be modulated by temperature and surface chemistry—has not yet been established. In particular, the origin of this second-order non-radiative component, and whether it is predominantly intrinsic (and thus unavoidable) or extrinsic (and potentially controllable), remains unclear. Nonetheless, they are regarded as the reason for a drop of ~50–100 mV in the open-circuit voltage (V_{oc}) of perovskite solar cells.[9] Therefore, understanding this recombination channel is crucial to guide strategies aimed at achieving the highest performance levels. For instance, elucidating the interplay between these non-typical second-order losses and classical first-order recombination will help in targeting the minimization of both losses, either independently or simultaneously, to enhance perovskite device performance.

Here, we present an approach to yield precise recombination parameters and, together with temperature-dependent measurements, we extract both k_1 and k_{2non} for various high-performance formamidinium lead iodide ($FAPbI_3$) variants. Using surface passivation methods as a lever, we demonstrate that the change in the radiative second-order recombination rate with temperature is in line with theoretically evaluated values. By contrast, we show that the absolute value of k_{2non} is an extrinsic parameter that relates to the surface, and the temperature-dependence of the values varies between samples. In our work, this extrinsic, surface-sensitive behavior of k_{2non}, together with density functional theory (DFT) calculations, supports its assignment to surface shallow trap states. Finally, utilizing the temperature-dependent recombination parameters, we calculate the practical impact on carrier losses for solar cell device open circuit voltage, V_{oc}, from sources of non-radiative recombinations via either k_1 or k_{2non}. The V_{oc} drop due to k_{2non} highlights the importance of eliminating the controllable k_{2non}, in addition to the more widely known and controllable k_1, when striving to reach the practical efficiency limits for perovskite solar cells.

II. RESULTS AND DISCUSSION

A. A joint TRPL–PLQE anchor separates the radiative and non-radiative components of k_2

A useful method to check film quality is by measuring recombination rates via time-resolved spectroscopy, such as TRPL. In several reports, arbitrary multi-exponential fitting is applied to the data to obtain a combination of two rates, but such approaches lack physical meaning (explained in supplementary material note 2) and thus are incapable of providing real recombination rates. Here, we employed an approach that is physically reasonable for representing the recombination processes and is mathematically logical for extracting the parameters. The rate equation for a photo-excited carrier population n, assuming uniform carrier density, can be described using a simplified equation

$$\frac{dn}{dt} = G - k_1 n - k_2 n^2 - k_3 n^3. \quad (1)$$

Here, the k_1, k_2, and k_3 represent the first, second, and third order (Auger) recombination rates, respectively. G is the generation term, which is time-independent for continuous excitation and time-dependent for pulsed laser excitation. Our measurements below explore two measurement conditions: pulsed excitation[11] and steady-

state excitation.[7] Under transient excitation, we solve Eq. (1) to obtain the PL intensity as a function of time,[11]

$$PL(t) = c\left(\frac{n_{init}k_1}{n_{init}k_2(e^{k_1 t}-1)+k_1 e^{k_1 t}}\right)^2. \quad (2)$$

Here, we neglect the Auger recombination term, which is negligible[12] under the excitation conditions used in our experiments. The n_{init} is the excited carrier density calculated by the recorded incident fluence, beam size, and film thickness. The constant c contains information about the photon collection efficiency of the instrument. We also assume lateral uniform excitation density over the sample and negligible charge transport effects for the time window over thousands of nanoseconds, supported by the ultrafast propagation and long diffusion lengths of carriers in perovskites.[13–15]

To measure and analyze recombination parameters, especially k_{2non}, we first deposit stabilized $FAPbI_3$ onto glass substrates, following a recipe using EDTA additives,[16] and the film sample is then treated with post-annealing in air for 24 h, and hereafter termed EDTA-24h. Next, we measure the TRPL decay curves with initial excitation densities generated from 520-nm-wavelength pulsed light from 5.2×10^{15} cm^{-3} to 2.3×10^{17} cm^{-3}. As shown in Fig. 1(a), we use Eq. (2) for global fitting on the excitation density-dependent TRPL traces. Here, global fitting means we input the excitation densities in a single step to fit all three traces simultaneously, and the only two variables are k_1 and k_2 as the variables, while c is a common constant representing the photon collection efficiency of the instrument. This method ensures a valid k_2 by globally matching the decays under high ($\sim 10^{17}$ cm^{-3}), medium ($\sim 10^{16}$ cm^{-3}), and low ($\sim 10^{15}$ cm^{-3}) excitation densities, including 1 sun illumination (equivalently between $\sim 10^{16}$–10^{17} cm^{-3}) and representing recombination, which is dominated by second-order, mixed-second, and first-order recombination regions, respectively. Moreover, the rate constant k_1 obtained via the global fitting (5.2×10^5 s^{-1}) is validated by an independent exponential fitting on the trace under the lowest excitation density (4.6×10^5 s^{-1}, supplementary material note 1, Table S1). The close agreement between these methods confirms the robustness of the global fitting, even as the system's complexity necessitates a multi-parameter analysis.

From the above fitting, we obtain the overall $k_2(2.44 \pm 0.03 \times 10^{-11}$ $cm^3 s^{-1})$, which is the coefficient representing all second-order recombination. To explore the components of k_2, we employ our recently developed photoluminescence quantum efficiency (PLQE)-based approach.[7] Typically, k_2 is interpreted as radiative from band-to-band recombination and thus is a constant value representing an intrinsic direct bandgap semiconductor property. Hence, k_{2r} and k_2 are not distinguished in the common definition of PLQE within the recombination model, as outlined

$$\eta_{PLQE} = \frac{\eta_{esc}k_{2r}(p_0 n + n^2)}{k_1 n + k_2 n^2 + k_3 n^3}. \quad (3)$$

Here, p_0 is the background hole concentration, which is negligible compared to carrier densities under 1 sun illumination for most lead-based perovskites, including those explored here (can be equally replaced in the case of n-doping by n_0).

We use Eq. (3) to fit the excitation density-dependent PLQE values, using a stochastic fitting strategy.[7] This method, applied to the PLQE values across a range of steady-state excitation densities spanning two orders of magnitude, extracts individual values for k_2 and $\eta_{esc}k_{2r}$. For this sample, the external PLQE has already dropped to $\sim 0.1\%$ at excitation densities about 50 times below 1 sun, and at lower fluence, the signal falls below our detection limit. To stabilize the PLQE–fluence fit and impose the physically required boundary condition that the PLQE vanishes as the excitation density tends to zero (radiative recombination $\propto np$ vs first-order SRH $\propto n$), we therefore introduce a single synthetic point at a fluence approximately 10^5 times lower than the lowest measured point and set its PLQE to zero. From the fitting as shown in Fig. 1(b) and Table S2, we obtain distinct values for $k_2(2.78 \times 10^{-11}$ cm^3 $s^{-1})$ and $\eta_{esc}k_{2r}(0.02 \times 10^{-11}$ cm^3 $s^{-1})$.

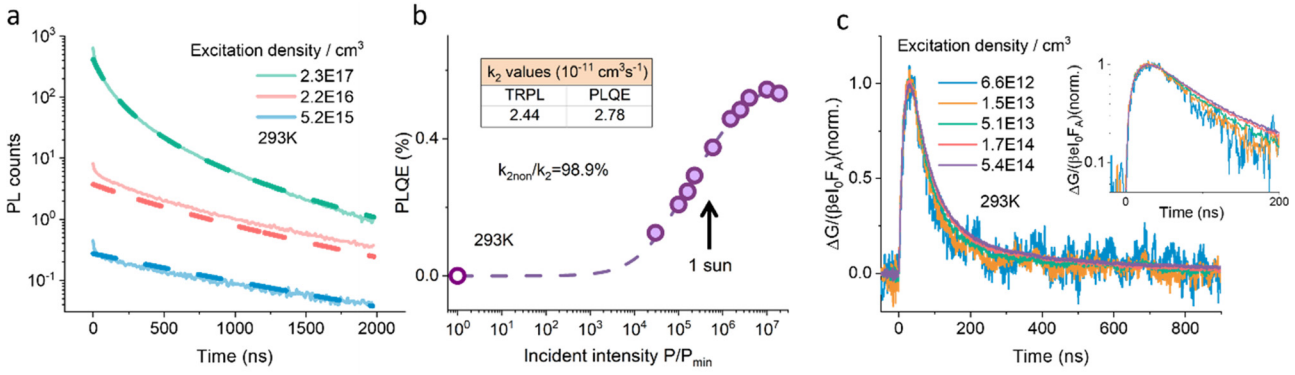

FIG. 1. Fits of TRPL and PLQE data acquired on thin films of $FAPbI_3$ EDTA-24h at room temperature. The fits exhibit agreement in the value of the overall second-order recombination rate, k_2, despite the different measurements and fitting models. (a) Excitation-density-dependent TRPL (solid lines) and fits (dashed lines). The excitation wavelength is 520 nm, and the repetition rate is 1 kHz. The k_2 value is double-checked by an exponential fitting of the trace at the lowest excitation density, shown in Fig. S1. (b) Excitation-density-dependent PLQE (solid symbols) and fits (dashed line) of PLQE using Eq. (3). The excitation wavelength is also 520 nm under continuous wave (CW) mode. The arrow points at the excitation density close to standard 1 sun illumination. The open symbol at the lowest excitation density is not a measured data point but a synthetic extremely-low-fluence point used only for the PLQE–fluence fit: we set the PLQE to zero at a fluence estimated to be five orders of magnitude below the lowest measured point in order to impose a boundary condition assumption that the PLQE tends to zero as the excitation density tends to zero. (c) Excitation-density-dependent TRMC traces normalized to 1, with excitation at 500 nm with a repetition rate of 10 Hz. Inset: log-linear plot of the traces.

While a hypothetical scenario could posit equality between these parameters (e.g., $k_2 = \eta_{esc}k_{2r}$), our unconstrained fitting procedure inherently yields non-identical values. This result indicates that such equality is neither required nor consistent with the data, allowing us to rule out this scenario. These values are listed in Table S1. Thereby, we confirm again that k_2 and $\eta_{esc}k_{2r}$ are different, subject to $k_2 = \eta_{esc}k_{2r} + k_{2non}$, accounting for both radiative and non-radiative processes. In planar, non-outcoupled films, where η_{esc} is small,[3] the fitted radiative product $\eta_{esc}k_{2r}$ can be small even when the intrinsic k_{2r} remains within literature-reported ranges for halide perovskites.[17] This is consistent with previous works in which distinct k_2 values are obtained by the same fitting method on transient absorption (TA) and TRPL, revealing the existence of the k_{2non} component. Herein, the k_{2non} values are obtained through the extracted k_2 and $\eta_{esc}k_{2r}$ values from Eq. (3).

While fitting PLQE data using Eq. (3), we need to input the value of k_1 to extract $\eta_{esc}k_{2r}$. To ensure accuracy, in addition to cross-verifying the k_1 value from the global fits via Eq. (2), we carried out time-resolved microwave photoconductivity (TRMC) measurements. These TRMC results confirm the first-order recombination regime, as illustrated in Fig. 1(c). Compared to recording radiative recombination of carriers by PL, TRMC records the overall recombination of free charge carriers, regardless of whether they recombine non-radiatively or radiatively. As shown in Fig. 1(c) inset, the TRMC decays show an overlapping and straight behavior under excitation densities in the range below 5.4×10^{14} cm^{-3}, where TRPL is no longer accessible from the instrument used in this study. In this range, the carrier recombination becomes non-radiative between trapped electrons and background holes, but with a rate (2×10^6 s^{-1}) larger than k_1 obtained from PL, indicating that PL is more influenced by surface traps since TRMC monitors residual mobile carriers in the bulk.[18] We herein continue to use TRPL for fitting but use TRMC as a cross-check.

Overall, our methodology employs two complementary pathways to determine k_2: the first uses Eq. (2) to globally fit TRPL data, providing a direct estimate of k_2 (alongside k_1, which is independently validated via exponential fitting), while the second and primary approach uses PLQE recordings [Eq. (3)], combined with the pre-determined k_1 values, to extract k_2 and further decouple it into its components, including the key parameter of interest, k_{2non}. While the TRPL fits serve as a useful cross-check for k_2, the PLQE + k_1 approach is the primary driver for obtaining k_2 and k_{2non}. Encouragingly, we find that, despite the different measurements and fitting models, the overall second-order recombination rate, k_2, obtained from the fitting approaches above is in good agreement: (2.44 ± 0.03) vs $(2.78 \pm 0.32) \times 10^{-11}$ cm^3 s^{-1} from TRPL and PLQE fitting respectively, as shown in Fig. 1(b). The low external PLQE of the planar test films is expected when η_{esc} is small and a residual k_{2non} is present and is therefore consistent with the extracted coefficients rather than indicative of a fitting artifact. Such values are consistent with previous results of k_2 from various time-resolved spectroscopies, such as THz spectroscopy,[17,19] TRMC,[18,20] TA,[3] and PL.[7] For example, they are within a single order of magnitude of $FAPbI_3$ values reported by OPTP/THz.[17] Specifically, optical-pump terahertz-probe (OPTP/THz) conductivity on $FAPbI_3$ thin films reports $\phi\, k_2 \approx (1.1 \pm 0.2) \times 10^{-10}$ cm^3 s^{-1};[17] by the same technique, $MAPbI_3$ typically yields $k_2 \approx$ (6–8) $\times 10^{-10}$ cm^{3}s^{-1} and $FAPbBr_3$ $k_2 \approx (1.0–1.2) \times 10^{-9}$ cm^3 s^{-1}.[6] These results, consistently falling within the range of $\sim 10^{-11} – 10^{-10}$ cm^3 s^{-1}, also align with simulations. This alignment, however, masks the potential existence of a non-radiative component (k_{2non}) within the total k_2, as the consistency implies completeness in the measured values. By combining global TRPL fitting (directly providing k_2 for cross-check and k_2) with stochastic PLQE fitting (decoupling k_2 into $\eta_{esc}k_{2r}$ and k_{2non} using k_1 values from global TRPL fitting, validated through exponential fitting), we extract $k_{2non} = 2.75 \times 10^{-11}$ cm^3 s^{-1} out of the total k_2 of 2.78×10^{-11} cm^3 s^{-1}. This reveals that k_{2non} dominates the total k_2 (98.9% for this sample), further consistent with the sample's low PLQE of around 0.4% at the excitation density equivalent to 1 sun.

B. Temperature-dependent analyses reveal that k_{2non} values are independent of k_1 and relate to an extrinsic property

To elucidate the origin of the non-radiative component of k_2 (i.e., k_{2non}), we carry out temperature-dependent measurements. As a prerequisite, we first examine the PL spectra of each sample under different temperatures, as shown in Fig. S2. The shift of the PL peak aligns with the change in the bandgap at lower temperatures, and the full width at half maximum (FWHM) of the PL peak becomes narrower. Importantly, no additional peak or shoulder emerges in the PL spectra at lower temperatures over the range studied here (50–293 K, Fig. S2), indicating that it is suitable for temperature-dependent analysis through either TRPL or PLQE.

To extract the k_2 values from both the TRPL and PLQE approaches at each temperature, we first record and carry out global fitting of TRPL traces at low temperatures, using Eq. (2), as shown in Figs. 2(a) and 2(c). Then, we record the PL emission spectra under the same excitation and signal collection conditions. This ensures an accurate ratio of PL spectra integration between low temperature and room temperature. Given no change in absorbance on temperature at the excitation wavelength (Fig. S2), and assuming that the ratio between PL emissions at two temperatures represents the ratio of PLQE at those temperatures,[7] we record the PL spectra at the excitation densities equivalent to those used in PLQE records. This allows us to obtain the excitation-density-dependent PLQE at each temperature, as shown in Figs. 2 and S4. We adopt this scaling method because direct PLQE measurements at low temperatures using integrating spheres are, in general, not feasible. We observe across the different samples that the PL emission intensity and consequently the PLQE increase at lower temperatures under the same excitation densities. Notably, most apparent at the lowest temperature, the excitation-density-dependent PLQE shows a downturn at high excitation densities, indicating the onset of Auger recombination. This onset is consistent with an increase in the Auger recombination rate and an increase in the carrier density due to reduced non-radiative recombination at low temperatures.[22]

At each temperature, we also record the TRMC traces to confirm first-order recombination behavior under the lowest excitation density. The temperature-dependent TRMC decays are shown in Fig. S5, and mobilities are in Fig. S6. At low temperatures, the first-order recombination rate becomes smaller, which is also in line with the rates obtained by TRPL. Similar to $MAPbI_3$, the sum of mobilities of free charge carriers, including electrons and holes, increases upon cooling, then drops at 150 K, which is close to the phase change temperature point of $FAPbI_3$.[19,23] This turning point indicates that the onset of

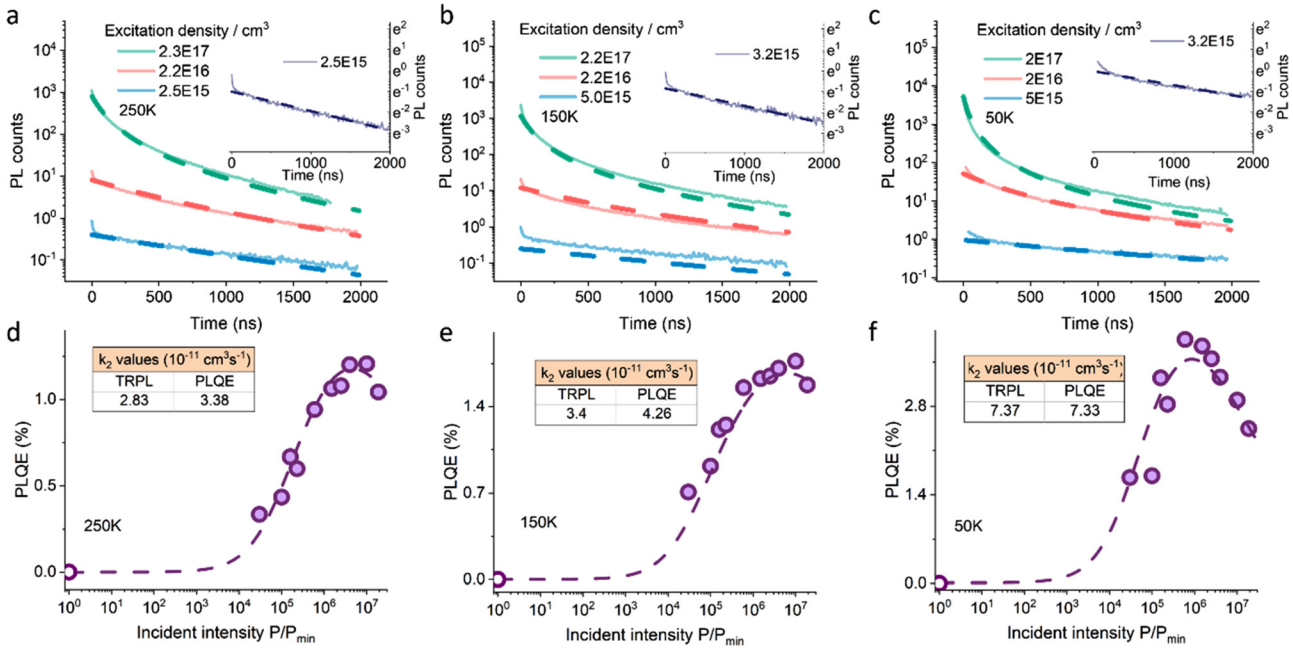

FIG. 2. Fits of TRPL and PLQE data obtained from $FAPbI_3$ EDTA-24h thin films at low temperatures. The estimated generation rate at the minimum excitation power, P_{min} in (d)–(f), is around 7×10^{16} cm^{-3} s^{-1}. Consistent k_2 values are obtained from the fits (dashed lines) of TRPL (solid lines) and PLQE (solid symbols) at each temperature, following the method applied at room temperature in Fig. 1, using Eqs. (2) and (3), respectively. The temperature-dependent traces of TRPL (a)–(c) are from direct recordings, while the low temperature PLQE (d)–(f) values are from scaling steady-state PL emission.[7,21] Results at other temperatures are shown in Figs. S3 and S4. Insets of (a)–(c): exponential fits (dashed lines) to the TRPL recorded (solid lines) under the lowest excitation density in ln-linear plots, with the excitation density stated (cm^{-3}). These linear fits ensure the validity of the k_1 values obtained from the global fitting.

Auger recombination at 150 K and lower arises from a combination of both reduced carrier trapping efficiency and mobility drop.

With these preparations, we apply the temperature-dependent analyses to the $FAPbI_3$ EDTA-24h sample. All recorded temperature-dependent TRPL traces of $FAPbI_3$ EDTA-24h are shown in full in Fig. S3, and a subset of spectra is shown in Figs. 2(a) and 2(c). At lower temperatures, we observe increasingly pronounced curvature of the TRPL traces across the whole range under high excitation densities, which is the excitation condition in which the second-order recombination dominates. Such a higher curvature indicates a larger value of k_2 at lower temperatures, and this is in line with previous temperature-dependent records and analysis of charge carrier dynamics, such as THz,[19] TRMC,[23] and TRPL.[24] As shown in Fig. S3, the global fitting method performs well across a range of parameters, accurately capturing decays with varying curvatures at different temperatures. For each temperature, the fitting was performed separately via the global fitting by Eq. (2). Additionally, the slope of the straight line in the log-linear plots, corresponding to first-order recombination, is smaller, suggesting a smaller value of k_1. These k_1 values are again double-checked (see Table. S1) by exponentially fitting the decay excluding the initial sharp drop, as shown in each inset in Figs. 2(a) and 2(c). Then, as with the room temperature data, we use these k_1 values to perform PLQE analysis at each temperature [Figs. 2(d) and 2(f)]. We find that the k_2 values obtained from TRPL by Eq. (2) and PLQE by Eq. (3) are consistent at each temperature. Based on the extracted k_2 values with good fits across all temperatures, we further find that k_{2non} value increases from 2.75×10^{-11} cm^3 s^{-1} to 6.8×10^{-11} cm^3 s^{-1} and k_{2non}/k_2 ratio drops from 98.9% to 92.9%.

We apply our fitting approach combining TRPL and PLQE on various $FAPbI_3$ samples, as shown in Figs. S3 and S4 and summarized in Table S4. We selected reagents from distinct materials chemistry classes to disentangle bulk vs surface contributions to k_{2non}. EDTA (multidentate Lewis base) is purported to chelate undercoordinated Pb^{2+} at grain interiors/boundaries, suppressing deep traps (bulk passivation). MACl (volatile chloride) is reported to transiently modulate crystallization and drives surfaces toward A-site–rich/near-stoichiometric terminations after annealing, allowing us to test the removal of PbI_2-like terminations without bulky capping. ACCl (quaternary ammonium) has been reported to steer the surface termination during growth while largely avoiding incorporation into the three-dimensional (3D) A-site lattice. Post-deposition CHABr and M-PEAI (bulky ammonium halides) are reported to form ultrathin quasi-2D surface layers that passivate halide vacancies and under-coordinated Pb at the outermost lattice.[25–27] Together, these choices span bulk passivation, growth/stoichiometry control, and explicit surface capping, allowing us to isolate how surface vs bulk chemistry governs k_{2non}. Specifically, we find (1) EDTA-std, a sample prepared using EDTA-doped precursors and surface-modified by gas quenching (standard method),[16] exhibits stable quality and has a k_{2non} of 9.75×10^{-11} cm^3 s^{-1} ($k_{2non}/k_2 = 97.5\%$); (2) EDTA-24h, the sample shown above in Figs. 1 and 2, treated with EDTA and post-annealed in air for 24 h at room atmosphere, exhibits stable

quality and an extended PL lifetime compared to the ETDA-std sample;[16] (3) MACl, prepared using an $FAPbI_3$ precursor treated with MACl and surface modification,[13] results in an improved polycrystalline morphology that enhances charge collection, achieving a solar cell efficiency of 23% with a much lower k_{2non} of 2.42×10^{-11} $cm^3\ s^{-1}$ and a k_{2non}/k_2 ratio of 75.6%; and (4) ACCl, a sample doped with ACCl and further surface-modified using CHABr and M-PEAI in IPA solution, results in a uniform, pinhole-free surface with large grains. This material attains the highest solar cell efficiency of 25.1%, with a k_{2non} of 2.68×10^{-11} $cm^3\ s^{-1}$ and a k_{2non}/k_2 ratio of 76.7%.

Despite the high qualities of either stability[16] or high device performance,[13] all samples exhibit significant k_{2non} values comparable to k_2 at room temperature. Previous work[20] using the combination of TRMC and PLQE analysis on perovskites verified that the overall k_2 can be affected by light-soaking post-treatment, highlighting the k_{2non} component, as k_{2r} is not expected to change since it is an intrinsic property. Here, we find different k_{2non} proportions in the different $FAPbI_3$ samples at room temperature, which are as large as around 98% ($k_{2non} = 9.75 \times 10^{-11}$ $cm^3\ s^{-1}$) in EDTA samples and still significant at 77% in ACCl ($k_{2non} = 2.68 \times 10^{-11}$ $cm^3\ s^{-1}$), which shows state-of-the-art solar cell performance. After cooling, as shown in Fig. S7, the k_2 values of all samples extracted from TRPL and PLQE are consistent at each temperature, allowing us to analyze the temperature-dependent trend of k_{2non} and k_1 values. As exhibited in Figs. 3(a) and 3(c) and Figs. S6–S8, which show the quantified temperature dependence of recombination rates, the trend of k_{2non} values on temperature does not follow either k_1 or k_2. This discrepancy means there is no straightforward relationship between k_{2non} and k_1 or mobility.

First, the k_1 values decrease as temperature decreases for all samples [Fig. 1(a)], in line with a previous study[19] on halide perovskites and conforming to the standard behavior of traditional semiconductors, such as recombination rates governed by deep traps.[28] The k_1 is traditionally described by a Shockley-Read-Hall model, and its decrease at low temperatures is attributed to reduced thermal energy, which diminishes impurity ionization, passivates dopant sites, and limits their role in recombination.[19] Meanwhile, the absolute k_1 value depends on the density and energy level position of traps. Therefore, due to the differences in doping and surfaces between the four samples, we observe a significant difference between the k_1 values, as seen in Fig. 3(a). Both MACl (7.7×10^5 s^{-1}) and ACCl (7.9×10^5 s^{-1}) samples, which are proven excellent solar cells, present significantly smaller k_1 than EDTA-std (7.8×10^6 s^{-1}). This suggests that bulk-doping modified film crystallization leads to fewer deep traps in the materials. The improved[13] surface effect is supported by the EDTA-24h, where the 24-h post-annealing in air primarily modifies the surface condition of the material compared to EDTA-std.[16] In this case, the k_1 of the EDTA sample drops dramatically (from 7.8×10^6 s^{-1} to 5.2×10^5 s^{-1}) and becomes comparable to that of MACl and ACCl.

Second, the k_2 values increase as the samples are cooled, in contrast to k_1, as shown in Fig. S7 for comparison. This increase aligns with previous experimental reports about k_2 in halide perovskites, using various time-resolved spectroscopies.[19] It also follows the trend of temperature-dependent theoretical calculations on k_2.[29] In Fig. S6, we plot $\eta_{esc}k_{2r}$ values of each sample, together with the simulated k_{2r} via the van Roosbroeck–Shockley relation, using temperature-dependent absorption (supplementary material note 2). Importantly, we find that the lines of $\eta_{esc}k_{2r}$ values for each sample as a function of temperature are exactly

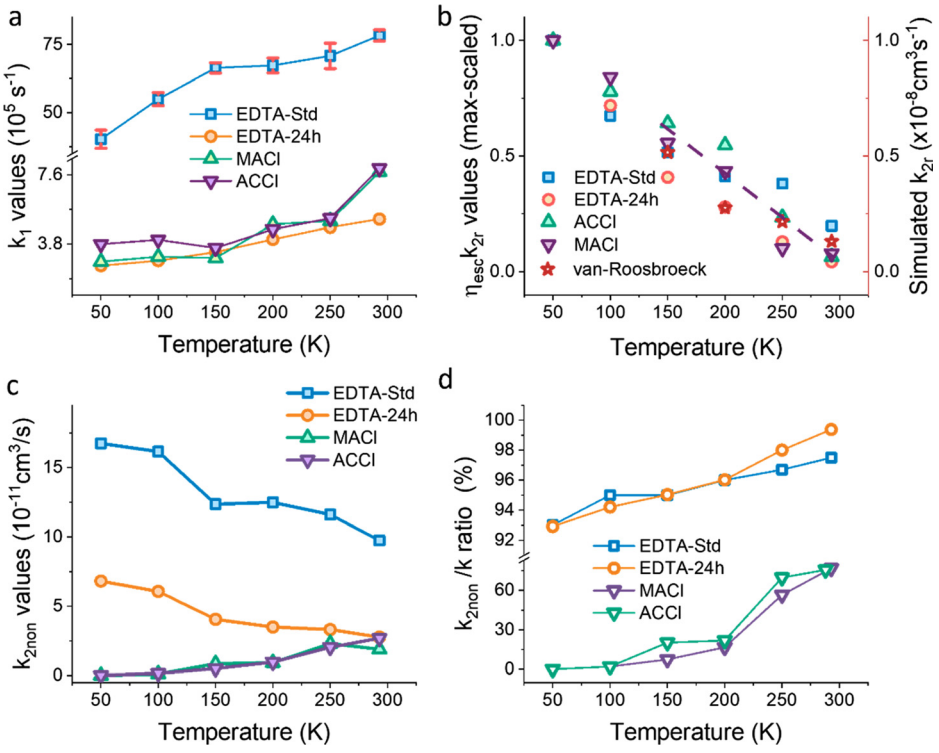

FIG. 3. Temperature-dependent recombination rates, extracted from fits to PLQE and TRPL data in Figs. 2, S3, and S4, using Eqs. (2) and (3) demonstrate the intrinsic and extrinsic properties of k_2. (a) k_1 values from TRPL fits, checked by exponential fits to the traces at the lowest excitation density. Error bars are representatively included for the EDTA-std sample. The error bar represents the standard error derived from the global fit covariance matrix, accounting for residual variance, data variability, and parameter correlations. Direct comparisons of $\eta_{esc}k_{2r}$ (b), k_{2non} (c), and k_{2non}/k_2 ratios (d) between different samples are derived from the approach in Sec. II A. Normalized temperature-dependent $\eta_{esc}k_{2r}$ values with a dashed line (guide to the eye) illustrating their parallel nature to the simulated k_{2r} derived from the van Roosbroeck–Shockley relation.

parallel to the line of the simulated k_{2r}. The vertical offsets between these parallel lines arise exclusively from variations in η_{esc}, a factor critically influenced by surface treatment that differs among the four samples due to fabrication parameters, and also the difference in thickness.[30]

To further explore the parallel nature of these lines, we independently normalized the extracted $\eta_{esc}k_{2r}$ values to their respective maxima [Fig. 3(b)]. This normalization shifts the curves vertically but preserves their temperature-dependent slopes, which were individually shown for all samples in Fig. S6. After scaling, the $\eta_{esc}k_{2r}$ values of the four samples—despite stark differences in doping, fabrication, and surface treatments—align onto the same line. This alignment reinforces that the temperature-dependent k_{2r}, extracted using Eq. (3), is an intrinsic property of $FAPbI_3$, while the pre-normalization vertical offsets exclusively reflect extrinsic, sample-dependent variations in η_{esc}. This follows the principle of detailed balance, which states that the radiation by recombination and generation by absorption of electron–hole pairs are equal at thermal equilibrium. This means that the intrinsic second-order recombination is the reverse process of absorption of charge carriers, as has been reported for $MAPbI_3$. According to the Van Roosbroeck–Shockley relation, the increase in k_{2r} during cooling can be attributed to the narrower Bose–Einstein distribution of electrons and holes, which increases the electron–hole interaction probability.[29]

Finally, as shown in Fig. 3(c), the trend of temperature-dependent k_{2non} is not clearly following either k_2 or k_1. By contrast, the k_{2non}/k_2 ratio is monotonically decreasing over temperature for all samples [Fig. 3(d)], regardless of the significant discrepancy in values. MACl and ACCl, which have the smallest k_1 and k_{2non}, also show a smaller k_{2non}/k_2 ratio, dropping from around 75% to nearly negligible when cooling to 50 K. This suggests that, in these samples, the increase in k_2 as the sample is taken to lower temperatures is mainly due to k_{2r}. Despite a clear decrease, both the EDTA-std and EDTA-24h samples maintain a large ratio of about 93% of k_{2non}/k_2 at 50 K. This implies that at 50 K, trap-assisted first-order recombination is the only carrier loss mechanism in MACl and ACCl, while k_{2non} still plays a significant role in the EDTA samples. Compared to the EDTA-std sample, the surface-modified EDTA-24h (post-treated) exhibits k_1 and k_2 values comparable to those of MACl and ACCl at room temperature. However, unlike MACl and ACCl, the k_{2non} of EDTA-24h still increases upon cooling, like EDTA-std. This means that in the case of EDTA-24h, of which the surface treatment is incomplete,[16] k_{2non} remains pronounced at room temperature and persists at lower temperatures. Meanwhile, since k_1 is already significantly depressed, this case of EDTA-24h reinforces that k_1 and k_{2non} are different.

Despite the same temperature-dependent trend of k_1 and k_{2non} of MACl and ACCl, the value of k_1 only drops two times while the k_{2non} reduces to a negligible value with respect to the absolute rates of other contributing terms with complete surface treatments, suggesting no connection between k_1 and k_{2non}. The distinction could indicate that k_{2non} arises from shallow states, unlike k_1 from deep traps. In shallow states, carriers are weakly localized, allowing them to escape back to the conduction or valence band via thermally activated processes.[31] This thermal localization enhances k_{2non} at lower temperatures, as cooling reduces carrier escape rates and increases state occupancy. However, this enhancement diminishes or even reverses if fewer carriers can be trapped—such as when the energy distribution and density of shallow states are substantially reduced. This is evidenced by Fig. 3(c): EDTA-std and EDTA-24h samples exhibit elevated k_{2non} at lower temperatures, while MACl and ACCl display suppressed k_{2non} values, owing to effective surface modification for the latter samples.

C. The origin of k_{2non} is attributed to surface shallow states

The results above show that k_{2non} is a substantial, extrinsic contribution to the second-order recombination that is strongly sensitive to surface treatments, whereas k_1 and k_{2r} behave as expected for deep-trap SRH and intrinsic radiative recombination. This suggests that k_{2non} may be linked to shallow surface states rather than deep bulk defects. In the growing work on shallow states in perovskites,[2,7,9,10,20] the non-radiative components of the bimolecular recombination coefficient are consistent with shallow band edge traps—especially those very close to the band edge—but this relationship is not made explicitly, and the origin is not clear.

Within the Shockley–Read–Hall (SRH) framework, $R = \frac{np - n_i^2}{\tau_p(n+n_t)+\tau_n(p+pt)}$. For shallow traps near the band edge under fast band–trap exchange, trap occupancy tracks free carriers; eliminating the trap variable yields an effective non-radiative bimolecular term $R_{\mathrm{nr}} \approx k_{2non}np$, with $k_{2non} \propto \sigma v_{\mathrm{th}} N_t$(thermal factors omitted for brevity). A detailed SRH-based derivation showing how shallow traps near the band edge can manifest as an effective non-radiative bimolecular channel is given in supplementary material note 1. Hence, fits to the simple first-/second-/third-order recombination rate equation [Eq. (1)] without an independent radiative anchor will absorb shallow-trap SRH into the empirical k_2.

In view of the physical processes described by SRH, in weakly trapping shallow states, electron–hole recombination resembles band-to-band processes in its dependence on both the concentration of electrons and holes, but becomes non-radiative due to the localization of one carrier. This second-order effect can be considered as an extreme case of the Shockley-Read-Hall recombination model with shallow traps. Our experimental results support this model over trap-assisted Auger recombination (TAAR), which, for example, leads to k_{2non}-type processes in III-nitride semiconductors.[32] TAAR is a pseudo-second-order process in which a trapped carrier is involved in the third-order Auger recombination. However, due to the trap density overwhelming the other two, the trapped concentration in the recombination form can be scaled into the coefficient, leading to a pseudo-second order expression. Representative cases of the TAAR process include a highly doped semiconductor, such as silicon,[33] or semiconductor nanocrystals.[34] The key common factors that lead to TAAR in these cases are high carrier density (from heavy doping or strong confinement) and high trap concentration (from doping or a large surface area to volume ratio). In our case, Auger recombination only appears at low temperatures in the recorded excitation density range (or at low temperature, the onset of Auger recombination shows up at lower densities), consistent with reduced carrier trapping and the change in mobility spike, but k_{2non}/k_2 is larger at room temperature, in contrast to the temperature-dependence of TAAR.[35,36] Also, the carrier density after excitation in our work is comparable to 1 sun illumination, which does not yield a high carrier concentration. Moreover, the opposite trend of temperature-dependent k_1 and k_{2non} in both EDTA-std and EDTA-24h suggests that the deep trap concentration is not directly involved in k_{2non} processes.

A relatively high concentration of trap density is possible at the surface or grain boundaries, where the density of states can differ from the bulk due to lattice termination. The k_{2non} values of the samples, labeled as EDTA-std for the bare film and EDTA-24h for film with surface modified after treatment, present a significant difference in Fig. 3(c), supporting the relevance of the surface. This is further supported by the other two samples, ACCl and MACl, both of which show much smaller k_{2non} with specific surface modification. The possibility of relatively concentrated surface traps also aligns with wider literature,[20,38,39] consistent with k_{2non} primarily being a surface effect. The light soaking effect, which enhanced PL lifetime and PLQE, was originally demonstrated in $MAPbI_3$ and was proposed to be effective on surface shallow states.[20] The same treatment on $FAPbI_3$ also led to better PL performance; meanwhile, bulk properties were not affected.[16]

To provide a microscopic realization of such shallow surface states, we next perform DFT calculations on different $FAPbI_3$ surface terminations (Fig. 4) and examine how the resulting shallow states are consistent with the experimentally observed k_{2non}. We stress that these DFT calculations are used to support the existence and qualitative character of shallow surface states for particular terminations; the quantitative recombination strengths reported in this work are experimentally measured as shown above and are not inferred directly from DFT. We find that in the case of PbI_2 surface terminations, $[PbI_6]^{4-}$ octahedra are truncated at the surface, thus creating an extra projected density of states to be 1.6×10^{13} cm^{-2} at the surface, spanned by a reference value of ~320 meV adjacent to the valence band. By contrast, for FAI-terminated surfaces, the $[PbI_6]^{4-}$ octahedra remain structurally intact with no truncation, as shown in Fig. S9. Consequently, no such extra projected density of states at the surface is observed in this configuration. Such a result resembles the energy levels of the surface states that are located just above the top of the valence band in bulk $MAPbI_3$.[30] Holes could accumulate in these shallow states, while electrons will remain in the bulk region.[31] One possible mechanism for k_{2non} is thus illustrated in Fig. 4(e). These locally accumulated holes, which hop between these surface states and bulk states, involve the overall carrier density in the valence band in their recombination, leading to a second-order recombination behavior but with a rate different from band-to-band. The shallow states responsible for k_{2non}, which arise intrinsically from the surface termination of PbI_2, support the ubiquitous presence of k_{2non} in lead halide perovskites.[7] Such surface termination-induced shallow states are in line with the experimental results that the surface-targeted treatment, either gas quenching or post-treatment, could effectively decrease k_{2non}.

Given that the shallow states are from the PbI_2 surface terminations, these states are localized and energetically distinct from bulk $FAPbI_3$ bands. At lower temperatures, some surface shallow states (on the deeper side) behave like deep traps because cooling reduces the thermal energy required for holes to escape back to the valence band. These states now act as deep hole traps, forcing recombination to proceed in the same as k_1. This reduces the k_{2non}/k_2 ratio because fewer active shallow traps contribute to k_{2non}, meanwhile k_{2r} increases. Although k_{2non}/k_2 ratio decreases at lower temperatures for all samples, the absolute k_{2non} values exhibit distinct trends: they increase for EDTA-std and EDTA-24h but decrease for surface-modified samples (MACl and ACCl). Notably, the k_{2non} reduction in surface-modified samples follows an exponential temperature dependence, consistent with an activation energy process. This behavior is corroborated by the Arrhenius plot in Fig. S10, which reveals an activation energy of ~40 meV. Such activation is consistent with trapping/detrapping in the shallow surface states identified for PbI_2-terminated surfaces; in this picture, variations in k_{2non} reflect changes in the capture pre-factor (effective capture cross-section and carrier thermal velocity) and, potentially, the effective activation term via electron–phonon coupling.[40] The presence of this energy barrier indicates that surface

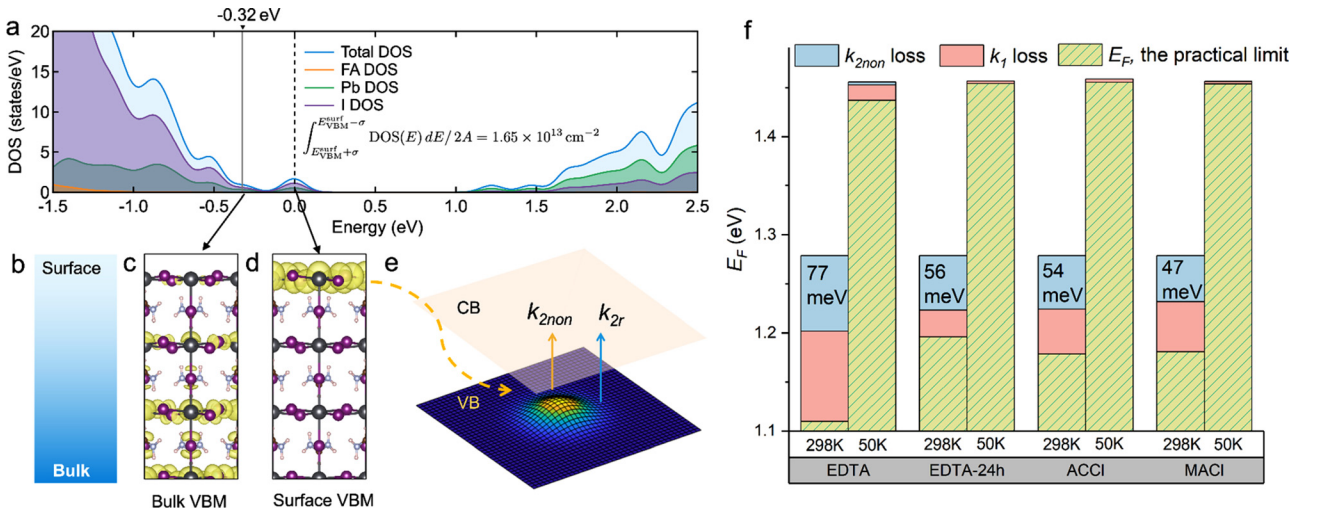

FIG. 4. (a)–(d) DFT calculations of PbI_2 termination at the surface. (a) Atom-/species-projected DOS (density of states) for the PbI_2-terminated surface slab, highlighting an additional distribution of surface states near the valence-band edge (b) shows the positions of calculated density of states from bulk toward surface for (c) and (d). As illustrated in (d), shallow states adjacent to the valence band, extending to a DFT-calculated reference value of ~320 meV, are generated by the surface termination of PbI_2. These surface shallow states act as a "collection bowl" for holes, thus leading to the k_{2non} process as depicted in (e), along with k_{2r}. (f) Calculated E_F at room temperature and 50 K. The k_{2non} loss contributes 47–77 meV of the overall carrier losses at ambient conditions and is nearly negligible at 50 K. The bar cap represents the detailed balance limit,[37] and the k_{2non} or k_1 loss is calculated by including or setting zero for the k_{2non} or k_1 values while determining the quasi-Fermi level splitting, E_F.

modification suppresses carrier recombination by introducing a kinetic hindrance. By contrast, EDTA-std (non-passivated) and EDTA-24h (partially modified) lack such an activation barrier. Their elevated k_{2non} at lower temperatures instead is solely dominated by thermal localization effects (reduced carrier escape, higher state occupancy). Given that PbI_2 terminations can be tailored via synthesis or post-treatment, these results highlight a viable pathway to control or even eliminate k_{2non} by engineering surface terminations.

Together with the VRS-anchored radiative component established above, the moderate carrier densities ($\sim 10^{16}\,cm^{-3}$) under ~1 sun and the temperature/fluence trends, including the ~40 meV passivation-activated suppression, show that the residual second-order channel in the regime studied is extrinsic and surface-sensitive. In this room-temperature, ~1-sun window, we therefore attribute k_{2non} primarily to shallow surface states and adopt a shallow-surface-trap extension of SRH/non-radiative multiphonon as the minimal microscopic picture consistent with the data; a III-nitride–type trap-assisted Auger mechanism or other multiparticle trap-mediated channels are not required to account for the observations and, if present, lie below the resolution of our measurements.

D. The quantified effect of k_{2non} on the open-circuit voltage of perovskite solar cells

Finally, independent of the DFT analysis, we evaluate the effect of k_{2non} on the practical performance of solar cells. In Fig. 4(c), we calculate the quasi-Fermi level splitting (i.e., difference in energy between the electron and hole populations after photoexcitation), E_F, calculated using the recombination rates and generation term from 1 sun illumination at AM1.5 (supplementary material note 3). Since E_F directly links to the open circuit voltage, V_{oc}, E_F can be taken as the practical limit of V_{oc}, as previously evaluated for perovskite solar cells.[41] As noted in the room temperature column for each sample, the loss due to k_{2non} contributes to as low as 47 meV (MACl) up to 77 meV (EDTA) of the total carrier losses. Even in-state-of-the-art devices such as ACCl (achieving a PCE of 25.1%), a residual energy loss of 54 meV persists. This underscores the need for targeted mitigation strategies from k_{2non}, despite significant breakthroughs in film quality and device optimization.

In line with the observation in Fig. 3 that k_{2non} and k_1 are not directly correlated, the losses associated with k_1 and k_{2non} differ in proportion, as shown in Fig. 4(f). The distinct E_F drop caused by k_1(1st-order, via deep traps) and k_{2non}(2nd-order, via shallow traps) underscores the two separate populations of traps and their fundamentally different recombination physics in solar cells. Both need addressing, and targeting the elimination of these losses is critical for device optimization. The observed reduction in the E_F caused by k_{2non}—when comparing the EDTA-std to the three other cases—underscores the potential of targeting surface conditions to mitigate k_{2non} losses and progress toward the radiative limits. Since additives can interact with PbI_2 during crystallization of $FAPbI_3$[25]—resulting in a smoother, more uniform surface—and the DFT simulation suggests that PbI_2 termination generates the shallow states, targeting terminations during and after crystallization presents a promising approach to further reducing k_{2non}. Moreover, we also evaluate E_F at 50 K with the parameter values obtained above. From the negligible effect of k_{2non} loss along with the decrease in k_1 loss upon cooling, we expect a much higher V_{oc}, approaching the theoretical limit, and thus better device performance under cooler conditions, such as those implemented in space applications.

III. CONCLUSIONS

In our work, we have elucidated the origins and impacts of the second-order non-radiative recombination pathway (k_{2non}), typically hidden in k_2 by the normally used simple first-/second-/third-order recombination rate equation, in halide perovskites. Specifically, our results— in line with studies of shallow states associated with k_{2non}, for which a clear physical origin had previously been lacking—provide evidence that k_{2non} arises from surface shallow states. By combining fluence- and temperature-dependent TRPL and PLQE and manipulating charge carrier dynamics through control of bulk and surface conditions, we reveal the radiative component ($\eta_{esc}k_{2r}$) of second-order recombination aligns with the simulated k_{2r} values from the Van Roosbroeck -Shockley relation as a function of temperature. We demonstrate that k_{2non} arises from shallow states, distinct from the first-order k_1 pathway mediated by deep traps. Both recombination pathways of carrier losses need to be addressed in device optimization strategies. Our analysis reveals that these shallow states are primarily governed by extrinsic factors, with PbI_2 terminations identified as a likely contributing factor through DFT calculations. Our further calculations show that the current gap between the best achieved V_{oc} to date and the limit, due to k_{2non} loss, is up to ~80 mV. This work not only enhances our understanding of k_{2non} but also provides actionable directions, emphasizing surface conditions to mitigate its effects, thereby paving the way for further improvements in perovskite solar cell efficiencies. Moreover, given k_{2non} loss is critical to address in single-junction cells; its impact remains equally vital when these wide gap cells are integrated into tandem architectures, as second-order non-radiative recombination directly weakens the luminescent coupling between sub-cells.[42,43]

SUPPLEMENTARY MATERIAL

See the supplementary material for the expanded information on sample fabrication for EDTA-std, EDTA-24h, MACl, and ACCl, and detailed descriptions of the PLQE, TRPL, TRMC, and temperature-dependent UV–VIS measurements. It further includes supporting tables that compile recombination parameters and lifetimes, theoretical notes on shallow-trap SRH recombination, k_2 and quasi-Fermi-level splitting calculations, and DFT methodology, as well as extended figures that illustrate the temperature-dependent photophysics and modeling results underpinning the conclusions of the main manuscript.

ACKNOWLEDGMENTS

The authors thank European Union's Horizon 2020 Research and Innovation Program, European Research Council, HYPERION, 756962 and PEROVSCI, 957513 (SDS, LD), the European Union's Horizon Europe Research and Innovation Program, European Research Council, VAPOURISE, 101169608 (SDS), EPSRC EP/V012932/1 (SDS, SN) and Sir Henry Royce Institute grant EP/R00661X/1 and EP/P024947/1 (SDS) CAM-IES grant EP/P007767/1 (SDS) European Research Council under the European Union's Horizon 2020 research and innovation program Grant Agreement No. SCORS – 101020167 (SG) Royal Society and Tata Group (Grant Nos. UF150033 and URF\R\221026) (SDS) Engineering and Physical Sciences Research Council EP/V06164X/1(LY, SDS) UKRI guarantee funding for Marie Skłodowska-Curie Actions Postdoctoral Fellowships 2021 (EP/X025756/1) (YKJ) and Leverhulme Research Grant RPG-2021-191

(SDS, YKJ). Emmanuel College, Cambridge for a Research Fellowship (SG). Swiss National Science Foundation Postdoctoral Fellowship TMPFP2_217040 (ARB).

AUTHOR DECLARATIONS

Conflict of Interest

Samuel D. Stranks is a co-founder of Swift Solar, Inc.

Author Contributions

Dengyang Guo: Conceptualization (equal); Data curation (lead); Formal analysis (lead); Investigation (lead); Methodology (equal); Writing – original draft (lead). **Satyawan Nagane:** Investigation (supporting); Methodology (supporting). **Stuart Macpherson:** Methodology (equal). **Weidong Xu:** Investigation (supporting); Methodology (supporting). **Jun Hong Noh:** Supervision (supporting). **Sang Il Seok:** Project administration (supporting); Resources (supporting); Supervision (supporting). **Tom Savenije:** Investigation (supporting); Project administration (supporting); Supervision (supporting); Writing – review & editing (supporting). **Samuel D. Stranks:** Conceptualization (equal); Funding acquisition (equal); Project administration (equal); Resources (equal); Supervision (equal); Writing – review & editing (equal). **Alan R. Bowman:** Conceptualization (supporting); Methodology (equal); Writing – review & editing (supporting). **Sebastian Gorgon:** Data curation (equal); Formal analysis (equal); Investigation (equal); Methodology (equal). **Changsoon Cho:** Methodology (supporting). **Young-Kwang Jung:** Data curation (equal); Formal analysis (equal); Investigation (equal); Methodology (equal); Writing – review & editing (supporting). **Jiashang Zhao:** Data curation (equal); Formal analysis (equal); Methodology (equal). **Linjie Dai:** Data curation (supporting); Formal analysis (supporting); Validation (equal). **Jaewang Park:** Investigation (supporting); Methodology (supporting). **Kyung Mun Yeom:** Investigation (supporting); Methodology (supporting).

DATA AVAILABILITY

The data that support the findings of this study are openly available in the University of Cambridge Apollo, Repository DOI: https://doi.org/10.17863/CAM.124659.

REFERENCES

[1]National Renewable Energy Laboratory, *Research Cell Record Efficiency Chart* (NREL, accessed Jul. 30, 2025).
[2]Y. Yuan, G. Yan, C. Dreessen, T. Rudolph, M. Hülsbeck, B. Klingebiel, J. Ye, U. Rau, and T. Kirchartz, "Shallow defects and variable photoluminescence decay times up to 280 μs in triple-cation perovskites," Nat. Mater. **23**(3), 391–397 (2024).
[3]J. M. Richter, M. Abdi-Jalebi, A. Sadhanala, M. Tabachnyk, J. P. H. Rivett, L. M. Pazos-Outón, K. C. Gödel, M. Price, F. Deschler, and R. H. Friend, "Enhancing photoluminescence yields in lead halide perovskites by photon recycling and light out-coupling," Nat. Commun. **7**(1), 13941 (2016).
[4]C. M. Wolff, S. A. Bourelle, L. Q. Phuong, J. Kurpiers, S. Feldmann, P. Caprioglio, J. A. Marquez, J. Wolansky, T. Unold, M. Stolterfoht, S. Shoaee, F. Deschler, and D. Neher, "Orders of recombination in complete perovskite solar cells–linking time-resolved and steady-state measurements," Adv. Energy Mater. **11**(45), 2101823 (2021).
[5]F. Staub, T. Kirchartz, K. Bittkau, and U. Rau, "Manipulating the net radiative recombination rate in lead halide perovskite films by modification of light out-coupling," J. Phys. Chem. Lett. **8**(20), 5084–5090 (2017).
[6]R. Brenes, D. Guo, A. Osherov, N. K. Noel, C. Eames, E. M. Hutter, S. K. Pathak, F. Niroui, R. H. Friend, M. S. Islam, H. J. Snaith, V. Bulović, T. J. Savenije, and S. D. Stranks, "Metal halide perovskite polycrystalline films exhibiting properties of single crystals," Joule **1**(1), 155–167 (2017).
[7]A. R. Bowman, S. Macpherson, A. Abfalterer, K. Frohna, S. Nagane, and S. D. Stranks, "Extracting decay-rate ratios from photoluminescence quantum efficiency measurements in optoelectronic semiconductors," Phys. Rev. Appl. **17**(4), 044026 (2022).
[8]R. L. Chin, A. M. Soufiani, P. Fassl, J. Zheng, E. Choi, A. Ho-Baillie, U. W. Paetzold, T. Trupke, and Z. Hameiri, "Surface saturation current densities of perovskite thin films from Suns-photoluminescence quantum yield measurements," Prog. Photovoltaics Res. Appl. **33**(1), 109–115 (2025).
[9]K. Hossain, D. Sivadas, D. Kabra, and P. R. Nair, "Perovskite solar cells dominated by bimolecular recombination—How far is the radiative limit?," ACS Energy Lett. **9**(5), 2310–2317 (2024).
[10]D. W. deQuilettes, K. Frohna, D. Emin, T. Kirchartz, V. Bulovic, D. S. Ginger, and S. D. Stranks, "Charge-carrier recombination in halide perovskites: Focus review," Chem. Rev. **119**(20), 11007–11019 (2019).
[11]S. Nagane, S. Macpherson, M. A. Hope, D. J. Kubicki, W. Li, S. D. Verma, J. Ferrer Orri, Y. Chiang, J. L. MacManus-Driscoll, C. P. Grey, and S. D. Stranks, "Tetrafluoroborate-induced reduction in defect density in hybrid perovskites through halide management," Adv. Mater. **33**(32), 2102462 (2021).
[12]C. Wehrenfennig, G. E. Eperon, M. B. Johnston, H. J. Snaith, and L. M. Herz, "High charge carrier mobilities and lifetimes in organolead trihalide perovskites," Adv. Mater. **26**(10), 1584–1589 (2014).
[13]C. Cho, S. Feldmann, K. M. Yeom, Y.-W. Jang, S. Kahmann, J.-Y. Huang, T. C. Yang, M. N. T. Khayyat, Y.-R. Wu, M. Choi, J. H. Noh, S. D. Stranks, and N. C. Greenham, "Efficient vertical charge transport in polycrystalline halide perovskites revealed by four-dimensional tracking of charge carriers," Nat. Mater. **21**(12), 1388–1395 (2022).
[14]J. Sung, C. Schnedermann, L. Ni, A. Sadhanala, R. Y. S. Chen, C. Cho, L. Priest, J. M. Lim, H.-K. Kim, B. Monserrat, P. Kukura, and A. Rao, "Long-range ballistic propagation of carriers in methylammonium lead iodide perovskite thin films," Nat. Phys. **16**(2), 171–176 (2020).
[15]E. M. Hutter, M. C. Gélvez-Rueda, A. Osherov, V. Bulović, F. C. Grozema, S. D. Stranks, and T. J. Savenije, "Direct–indirect character of the bandgap in methylammonium lead iodide perovskite," Nat. Mater. **16**(1), 115–120 (2017).
[16]T. A. S. Doherty, S. Nagane, D. J. Kubicki, Y.-K. Jung, D. N. Johnstone, A. N. Iqbal, D. Guo, K. Frohna, M. Danaie, E. M. Tennyson, S. Macpherson, A. Abfalterer, M. Anaya, Y.-H. Chiang, P. Crout, F. S. Ruggeri, S. Collins, C. P. Grey, A. Walsh, P. A. Midgley, and S. D. Stranks, "Stabilized tilted-octahedra halide perovskites inhibit local formation of performance-limiting phases," Science **374**(6575), 1598–1605 (2021).
[17]W. Rehman, R. L. Milot, G. E. Eperon, C. Wehrenfennig, J. L. Boland, H. J. Snaith, M. B. Johnston, and L. M. Herz, "Charge-carrier dynamics and mobilities in formamidinium lead mixed-halide perovskites," Adv. Mater. **27**(48), 7938–7944 (2015).
[18]D. Guo, D. Bartesaghi, H. Wei, E. M. Hutter, J. Huang, and T. J. Savenije, "Photoluminescence from radiative surface states and excitons in methylammonium lead bromide perovskites," J. Phys. Chem. Lett. **8**(17), 4258–4263 (2017).
[19]R. L. Milot, G. E. Eperon, H. J. Snaith, M. B. Johnston, and L. M. Herz, "Temperature-dependent charge-carrier dynamics in $CH_3NH_3PbI_3$ perovskite thin films," Adv. Funct. Mater. **25**(39), 6218–6227 (2015).
[20]T. J. Savenije, D. Guo, V. M. Caselli, and E. M. Hutter, "Quantifying charge-carrier mobilities and recombination rates in metal halide perovskites from time-resolved microwave photoconductivity measurements," Adv. Energy Mater. **10**(26), 1903788 (2020).
[21]S. D. Stranks, V. M. Burlakov, T. Leijtens, J. M. Ball, A. Goriely, and H. J. Snaith, "Recombination kinetics in organic-inorganic perovskites: Excitons, free charge, and subgap states," Phys. Rev. Appl. **2**(3), 034007 (2014).
[22]M. J. Trimpl, A. D. Wright, K. Schutt, L. R. V. Buizza, Z. Wang, M. B. Johnston, H. J. Snaith, P. Müller-Buschbaum, and L. M. Herz, "Charge-carrier trapping and radiative recombination in metal halide perovskite semiconductors," Adv. Funct. Mater. **30**(42), 2004312 (2020).
[23]J. Zhao, X. Liu, Z. Wu, B. Ibrahim, J. Thieme, G. Brocks, S. Tao, L. J. Bannenberg, and T. J. Savenije, "Temperature-dependent interplay between

structural and charge carrier dynamics in CsMAFA-based perovskites," Adv. Funct. Mater. **34**(13), 2311727 (2024).
[24]C. Wehrenfennig, M. Liu, H. J. Snaith, M. B. Johnston, and L. M. Herz, "Charge carrier recombination channels in the low-temperature phase of organic-inorganic lead halide perovskite thin films," APL Mater. **2**(8), 081513 (2014).
[25]J. Park, J. Kim, H.-S. Yun, M. J. Paik, E. Noh, H. J. Mun, M. G. Kim, T. J. Shin, and S. I. Seok, "Controlled growth of perovskite layers with volatile alkylammonium chlorides," Nature **616**(7958), 724–730 (2023).
[26]J.-W. Lee, Z. Dai, T.-H. Han, C. Choi, S.-Y. Chang, S.-J. Lee, N. De Marco, H. Zhao, P. Sun, Y. Huang, and Y. Yang, "2D perovskite stabilized phase-pure formamidinium perovskite solar cells," Nat. Commun. **9**(1), 3021 (2018).
[27]P. Li, Y. Zhang, C. Liang, G. Xing, X. Liu, F. Li, X. Liu, X. Hu, G. Shao, and Y. Song, "Phase pure 2D perovskite for high-performance 2D–3D heterostructured perovskite solar cells," Adv. Mater. **30**(52), 1805323 (2018).
[28]J. R. Haynes and J. A. Hornbeck, "Trapping of minority carriers in silicon. II. *n*-type silicon," Phys. Rev. **100**(2), 606–615 (1955).
[29]C. L. Davies, M. R. Filip, J. B. Patel, T. W. Crothers, C. Verdi, A. D. Wright, R. L. Milot, F. Giustino, M. B. Johnston, and L. M. Herz, "Bimolecular recombination in methylammonium lead triiodide perovskite is an inverse absorption process," Nat. Commun. **9**(1), 293 (2018).
[30]E. M. Hutter, "Perovskite escape room: Which photons leave the film, and which are trapped inside?," Chem **7**(4), 845–846 (2021).
[31]A. D. Wright, R. L. Milot, G. E. Eperon, H. J. Snaith, M. B. Johnston, and L. M. Herz, "Band-tail recombination in hybrid lead iodide perovskite," Adv. Funct. Mater. **27**(29), 1700860 (2017).
[32]A. C. Espenlaub, D. J. Myers, E. C. Young, S. Marcinkevičius, C. Weisbuch, and J. S. Speck, "Evidence of trap-assisted Auger recombination in low radiative efficiency MBE-grown III-nitride LEDs," J. Appl. Phys. **126**(18), 184502 (2019).
[33]S. K. Pang, A. W. Smith, and A. Rohatgi, "Effect of trap location and trap-assisted Auger recombination on silicon solar cell performance," IEEE Trans. Electron Devices **42**(4), 662–668 (1995).
[34]A. W. Cohn, A. M. Schimpf, C. E. Gunthardt, and D. R. Gamelin, "Size-dependent trap-assisted Auger recombination in semiconductor nanocrystals," Nano Lett. **13**(4), 1810–1815 (2013).
[35]V. B. Khalfin, M. V. Strikha, and I. N. Yassievich, "Auger recombination of electrons via deep and shallow acceptors," Phys. Status Solidi B **132**(1), 203–217 (1985).
[36]M. B. Johnston and L. M. Herz, "Hybrid perovskites for photovoltaics: Charge-carrier recombination, diffusion, and radiative efficiencies," Acc. Chem. Res **49**(1), 146 (2016).
[37]W. Shockley and H. J. Queisser, "Detailed balance limit of efficiency of p-n junction solar cells," J. Appl. Phys. **32**(3), 510–519 (1961).
[38]S. D. Stranks, G. E. Eperon, G. Grancini, C. Menelaou, M. J. P. Alcocer, T. Leijtens, L. M. Herz, A. Petrozza, and H. J. Snaith, "Electron-hole diffusion lengths exceeding 1 micrometer in an organometal trihalide perovskite absorber," Science **342**(6156), 341–344 (2013).
[39]D. W. deQuilettes, J. J. Yoo, R. Brenes, F. U. Kosasih, M. Laitz, B. D. Dou, D. J. Graham, K. Ho, Y. Shi, S. S. Shin, C. Ducati, M. G. Bawendi, and V. Bulović, "Reduced recombination via tunable surface fields in perovskite thin films," Nat. Energy **9**(4), 457–466 (2024).
[40]A. Alkauskas, Q. Yan, and C. G. Van De Walle, "First-principles theory of nonradiative carrier capture via multiphonon emission," Phys. Rev. B **90**(7), 075202 (2014).
[41]D. Guo, V. M. Caselli, E. M. Hutter, and T. J. Savenije, "Comparing the calculated Fermi level splitting with the open-circuit voltage in various perovskite cells," ACS Energy Lett. **4**(4), 855–860 (2019).
[42]A. R. Bowman, M. Anaya, N. C. Greenham, and S. D. Stranks, "Quantifying photon recycling in solar cells and light-emitting diodes: Absorption and emission are always key," Phys. Rev. Lett. **125**(6), 067401 (2020).
[43]A. R. Bowman, F. Lang, Y.-H. Chiang, A. Jiménez-Solano, K. Frohna, G. E. Eperon, E. Ruggeri, M. Abdi-Jalebi, M. Anaya, B. V. Lotsch, and S. D. Stranks, "Relaxed current matching requirements in highly luminescent perovskite tandem solar cells and their fundamental efficiency limits," ACS Energy Lett. **6**(2), 612–620 (2021).